# CHANNEL ESTIMATION AND PREDICTION IN WIRELESS COMMUNICATIONS ASSISTED BY SEMI-PASSIVE RIS

Mirza A. Haider<sup>1</sup>, Yimin D. Zhang<sup>1</sup>, and Elias Aboutanios<sup>2</sup>

 Department of Electrical and Computer Engineering, Temple University, Philadelphia, PA 19122, USA
 School of Electrical Engineering and Telecommunications, University of New South Wales, Sydney, Australia 2052

#### ABSTRACT

When the line-of-sight between the base station and mobile users is unavailable, reconfigurable intelligent surfaces (RIS) can be exploited to ensure connectivity and improve data transmission performance. The objective of this paper is to estimate and predict timevarying user-RIS channels with low pilot overhead using a small number of sparsely distributed active RIS elements. Structured covariance matrix interpolation is performed to fully utilize the array aperture from the sparse semi-passive RIS. Channel variation over time due to user movement and environmental factors can make it difficult to utilize all time slots for channel estimation and data transmission. To address this challenge, we propose a model based on long short-term memory (LSTM) networks for channel estimation and prediction to reduce the required training pilot signals and increase the transmission data rate using parallel computation. Simulation results verify the capability of the proposed approach to enhance data transmission in wireless networks and demonstrate its effectiveness compared to other machine learning models.

*Index Terms*— Reconfigurable intelligent surface, sparse array, structured matrix completion, channel estimation, machine learning.

# 1. INTRODUCTION

The emerging technology of reconfigurable intelligent surface (RIS) shows great potential for 5G and beyond due to its capability to modify wireless channels between communicating nodes. RIS is essentially a rectangular metasurface consisting of numerous passive reflecting elements, each of which can be digitally adjusted to cause a unique change in amplitude and/or phase shift of the incoming signal [1-3]. Compared to traditional relay technology, RIS offers significant advantages, such as achieving noise-free full-duplex passive beamforming/reflection while consuming much less power and having a lower implementation cost [4-6]. Optimal passive beamforming at the RIS requires accurate acquisition of the channel state information (CSI). To achieve high-precision performance for channel estimation, wireless channel reconfiguration, and pilot overhead reduction, it has been found effective to include a small number of active elements with sensing capabilities in the RIS [7-9]. In so doing, the RIS becomes more capable to improve signal parameter estimation, especially when subspace-based direction-of-arrival (DOA) estimation methods, such as MUSIC and ESPRIT, are used [7,9,10]. Specifically, exploiting the structural deployment of sparse active RIS elements has additional benefits for channel estimation, such as requiring fewer training data and enabling secure connectivity, user localization, and target recognition [11-13]. The effectiveness of

The work of M. A. Haider and Y. D. Zhang was supported in part by National Science Foundation (NSF) under Grant No. ECCS-2236023.

semi-passive RIS-assisted channel estimation has been demonstrated in [7] using randomly distributed sparse active RIS elements exploiting compressive sensing and machine learning techniques. It has been recently shown that accurate CSI estimation can be achieved by placing active elements on rectangular RIS structures in a certain way, such as a sparse L-shaped configuration with low or no redundancies in their lags [9, 14].

The rapid variation of the wireless channels due to user movement, environmental changes, and other factors requires continuous channel estimation and thereby compromises the data transmission efficiency. In [15], recurrent neural network (RNN) based predictors were proposed to combat outdated CSI caused by fast-changing multipath fading channels in adaptive transmission systems, utilizing long short-term memory (LSTM) or gated recurrent unit (GRU) for time-series prediction. LSTM has been extensively used for predicting sequential data by recursively forwarding past information to the current cell memory, as it can learn the long-term dependency of input data [16, 17].

The objective of this paper is to estimate and predict timevarying user-RIS channels with a lower pilot overhead using a small number of sparsely distributed active RIS elements. Toward this end, we first estimate the fast-fading multipath channel between the mobile user and the semi-passive RIS equipped with an L-shaped sparse array of active elements. The structured matrix completion technique is exploited to achieve superior DOA estimation performance with an increased number of degrees of freedom. We then predict the CSI over time by utilizing an LSTM-based RNN model. During the prediction, the base station (BS) can predict the channel without uplink pilots so the proposed method reduces the overhead of channel estimation by using fewer pilot symbols, allowing for more data transmission. To assess the efficiency of the prediction model, we compare it with a multilayer perceptron (MLP) network which forecasts the subsequent channel based on previous estimates of the RIS-user channels. Simulation results verify the effectiveness of the proposed technique in increasing transmission data time between the BS and mobile users via the RIS and its superiority compared to MLP-based approaches.

Notations: We use lower-case and upper-case bold characters to denote vectors and matrices, respectively. In particular,  $\mathbf{I}_N$  denotes the  $N \times N$  identity matrix.  $(\cdot)^T$  and  $(\cdot)^H$  respectively stand for the transpose and Hermitian operations of a matrix or a vector, whereas  $(\cdot)^\dagger$  returns the pseudo-inverse of a matrix.  $\mathrm{Tr}(\cdot)$  is the trace operator,  $\mathrm{diag}(\cdot)$  forms a diagonal matrix from a vector, and  $\otimes$  denotes Kronecker product.  $\|.\|_*$  and  $\|.\|_F$  respectively denote the nuclear and Frobenius norms of a matrix.  $\mathbf{A} \succcurlyeq 0$  indicates that matrix  $\mathbf{A}$  is positive semidefinite. Moreover,  $\mathbb{E}[\cdot]$  denotes statistical expectation, and  $\mathbb{C}^{M \times N}$  denotes the complex space with dimension  $M \times N$ .

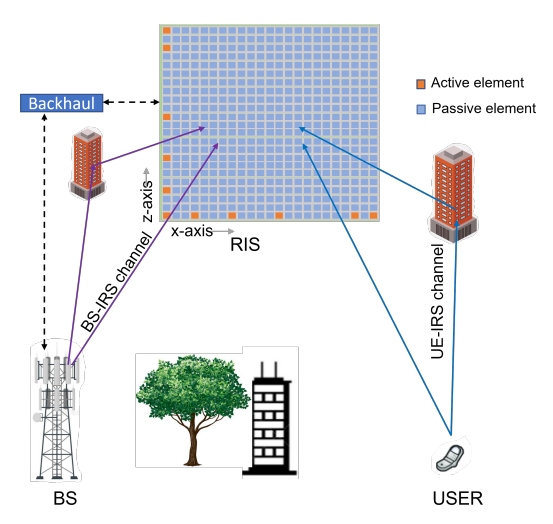


Fig. 1: Channel model of an RIS-assisted communication system.

#### 2. SYSTEM MODEL

Consider a multiple-input single-output (MISO) downlink communication system that includes a semi-passive RIS which consists of a small number of active elements, whereas the other elements are passive. The RIS assists in communication between a BS equipped with  $N_b$  antennas and a single-antenna user as shown in Fig. 1. The RIS is constructed as a uniform planar array, featuring a total of  $M = M_x \times M_z$  elements. This deployment is particularly suited for scenarios where the user is substantially obstructed from connecting with the BS. The M active elements among the total MRIS elements have active sensing as well as passive reflecting abilities. The arrangement of these active elements follows a sparsely distributed L-shaped pattern. This pattern involves an  $\bar{M}_x$ -element subarray placed horizontally along the x-axis and an  $\bar{M}_z$ -element subarray oriented vertically along the z-axis. It is noted that the total number of active RIS elements is  $\bar{M} = \bar{M}_x + \bar{M}_z - 1$  because the corner element is shared by both subarrays.

The two-dimensional steering vector  $\mathbf{a}_{RIS}(\vartheta,\varphi)$  of the entire planar RIS is expressed as [18]

$$\mathbf{a}_{RIS}(\vartheta,\varphi) = \mathbf{a}_x(\vartheta,\varphi) \otimes \mathbf{a}_z(\vartheta), \tag{1}$$

where the steering vectors  $\mathbf{a}_x(\vartheta,\varphi)$  and  $\mathbf{a}_z(\vartheta)$  are respectively associated with the horizontally and vertically oriented subarrays, respectively expressed as

$$\mathbf{a}_{x}(\vartheta,\varphi) = [1, e^{-j\frac{2\pi}{\lambda}d\sin(\vartheta)\sin(\varphi)}, \\ \dots, e^{-j\frac{2\pi}{\lambda}d(M_{x}-1)\sin(\vartheta)\sin(\varphi)}]^{\mathrm{T}},$$
(2)

$$\mathbf{a}_{z}(\vartheta) = \left[1, e^{-j\frac{2\pi}{\lambda}d\cos(\vartheta)}, \dots, e^{-j\frac{2\pi}{\lambda}d(M_{z}-1)\cos(\vartheta)}\right]^{\mathrm{T}}.$$
 (3)

where  $\varphi$  represents the azimuth angle,  $\vartheta$  denotes the elevation angle, and  $\lambda$  stands for the wavelength. The inter-element spacing between the RIS elements, given by d, is consistent across both the x-axis and z-axis subarrays. The channel vector  $\mathbf{h}$  of the link between the RIS and the mobile user results from the cumulative effect of L distinct paths and is given as

$$\mathbf{h} = \sum_{l=1}^{L} \beta_l \mathbf{a}_{RIS}(\vartheta_l, \varphi_l), \tag{4}$$

where  $\beta_l$  is path gain of the lth path for  $l=1,2\cdots,L$ , and  $(\varphi_l,\vartheta_l)$  is the associated angle pair.



Fig. 2: The transmission frame structure.

The conceptual framework for channel detection and prediction is illustrated in Fig. 2, with B denoting the input order. As the mobile user moves relative to the RIS, the CSI between the two will continuously change. However, for the short time period  $t = 1, 2, \dots, T$ in each time frame  $T_n = T - n + 1$ , where  $n = B, B - 1, \dots, 1$ , the channel variation is considered insignificant. During each time frame,  $T_n$ , there are two modes: sensing and data transmission. In the sensing mode, the mobile user sends uplink pilot signals while the RIS estimates the channel using its active elements. In the data transmission mode, the BS sends downlink data to the mobile user through the channel estimated by the RIS. More specifically, during the uplink sensing mode, the active RIS elements collect  $\dot{T}$  pilot samples for each time frame and forward them to the BS through a backhaul network so that the user-RIS channel  $\mathbf{h}_{T_n} \in \mathbb{C}^{M \times 1}$  can be estimated. For the data transmission phase, the RIS switches to the reflection mode, and all RIS elements are used to reflect signals from the BS to the mobile user or vise versa for data transmission, referred to as "Data Tx" in Fig. 2.

# 3. PROPOSED CHANNEL ESTIMATION AND PREDICTION METHOD

In addition to these conventional phases, we consider that the BS employs the LSTM networks to predict the subsequent channel for the (T+1)th time frame. In this section, we respectively present the channel estimation and prediction steps in two subsections.

### 3.1. RIS-Assited User-RIS Channel Estimation

The multipath channel between the mobile user and RIS is estimated using the active RIS elements during the training phase. We adopt the optimized hybrid non-redundant array (ONRA) structure for both horizontal and vertical subarrays [14, 19]. These active RIS subarrays positioned along the x- and z-axes are respectively denoted as  $\mathbb{X}=\{p_0,p_1,\cdots,p_{\bar{M}_x-1}\}\lambda/2$  and  $\mathbb{Z}=\{q_0,q_1,\cdots,q_{\bar{M}_z-1}\}\lambda/2$ , where  $p_i$  and  $q_i$  are integers for all i, and  $p_0=q_0=0$  is assumed. Furthermore, we define  $W_x=p_{\bar{M}x-1}+1$  and  $W_z=p_{\bar{M}z-1}+1$  as the lengths encompassing active and passive elements within the respective subarray apertures. The uplink signal received at the active RIS elements comprises L uncorrelated narrowband multipath components that arrive at the RIS from DOAs  $(\vartheta_l,\varphi_l)$  for  $l=1,\cdots,L$ .

Let  $\mathbf{x}(t)$  and  $\mathbf{z}(t)$  denote the received signals at time  $t = 1, \dots, \dot{T}$  at the x-axis and z-axis subarrays, respectively, expressed as [10, 18]:

$$\mathbf{x}(t) = \sum_{l=1}^{L} \beta_l \tilde{\mathbf{a}}_x(\varphi_l, \vartheta_l) s_u(t) + \mathbf{n}_x(t), \tag{5}$$

$$\mathbf{z}(t) = \sum_{l=1}^{L} \beta_l \tilde{\mathbf{a}}_z(\vartheta_l) s_u(t) + \mathbf{n}_z(t), \tag{6}$$

where  $s_u(t) = \sqrt{P}s(t)$  is the uplink signal, P represents the transmitted power, and s(t) is normalized transmit signal such that  $\mathbb{E}(|s(t)|^2) = 1$ . The steering vectors of the two subarrays along the x and z axes are respectively denoted as  $\tilde{\mathbf{a}}_x(\vartheta_l,\varphi_l) \in \mathbb{C}^{W_x \times 1}$  and  $\tilde{\mathbf{a}}_z(\vartheta_l) \in \mathbb{C}^{W_z \times 1}$ . The noise vectors  $\mathbf{n}_x(t)$  and  $\mathbf{n}_z(t)$  represent

the additive white Gaussian noise (AWGN) in the two subarrays. Note in (5) and (6) that  $\tilde{\mathbf{a}}_z(\vartheta_l)$  and  $\tilde{\mathbf{a}}_z(\vartheta_l)$  and, subsequently,  $\mathbf{x}(t)$  and  $\mathbf{z}(t)$ , are defined in  $W_x$ - and  $W_z$ -sensor uniform linear array (ULA) positions, and their elements corresponding to missing sensor positions take a zero value.

For each time frame of length  $\dot{T}$ , we first perform the DOA estimation of the received signals at the vertical subarray, and the received signals are organized into the following matrix form

$$\mathbf{Z} = [\mathbf{z}(1), \mathbf{z}(2), \cdots, \mathbf{z}(\dot{T})] \in \mathbb{C}^{W_z \times \dot{T}}.$$
 (7)

Assuming that the noise samples are mutually independent and also uncorrelated with the signals, the covariance matrix of  $\mathbf{z}(t)$  is obtained as

$$\tilde{\mathbf{R}}_{z_{\text{RIS}}} = \mathbf{Z}\mathbf{Z}^{\text{H}} = \tilde{\mathbf{A}}_{z}\mathbf{R}_{s}\tilde{\mathbf{A}}_{z}^{\text{H}} + \sigma_{n}^{2}\mathbf{U}_{z}\mathbf{U}_{z}^{\text{H}}, \tag{8}$$

where  $\mathbf{R}_s = \mathrm{diag}(\sigma_1^2, \sigma_2^2, \cdots, \sigma_L^2), \, \sigma_l^2$  represents the power of the signal from the l-th path,  $\sigma_n^2$  denotes the noise power, and  $\mathbf{U}_z \in \mathbb{C}^{W_z \times M_z}$  is a binary diagonal mask matrix representing the presence of antennas in the z-axis subarray, given as  $[\mathbf{U}_z]_{g,g} = 1$  if  $g\lambda/2 \in \mathbb{Z}$  and 0 otherwise.

Due to the sparse arrangement of the active RIS elements, the covariance matrix  $\tilde{\mathbf{R}}_{z_{\mathrm{RIS}}}$  contains holes in the half-wavelength space. In order to derive the covariance matrix for the ULA positioned along the z-axis, we leverage the widely recognized matrix interpolation approach. This technique involves interpolating  $\tilde{\mathbf{R}}_{z_{\mathrm{RIS}}}$  by solving a nuclear norm or rank minimization problem [20–22].

Denote the interpolated covariance matrix as  $\hat{\mathbf{R}}_{z_{\mathrm{RIS}}}$ . We apply the MUSIC algorithm to  $\hat{\mathbf{R}}_{z_{\mathrm{RIS}}}$  to estimate the elevation DOAs of the user-RIS multipath signals. The array manifold matrix  $\mathbf{A}_z(\hat{\theta}) = [\mathbf{a}_z(\hat{\theta}_1), \mathbf{a}_z(\hat{\theta}_2), \cdots, \mathbf{a}_z(\hat{\theta}_L)] \in \mathbb{C}^{M_z \times L}$  for the z-axis subarray can then be constructed based on the estimated elevation angles.

When estimating azimuth angles, it is crucial to match them with their corresponding elevation angles. Leveraging the interconnections among the components encompassing the signal subspace leads to the estimation of  $\mathbf{R}_{\mathbf{S}}$  as

$$\hat{\mathbf{R}}_{s} = \mathbf{A}_{z}^{\dagger}(\hat{\theta})\hat{\mathbf{V}}_{zs}(\hat{\mathbf{\Gamma}}_{z} - \sigma_{n}^{2}\mathbf{I}_{L})\hat{\mathbf{V}}_{zs}^{H}(\mathbf{A}_{z}^{\dagger}(\hat{\theta}))^{H}, \tag{9}$$

where  $\hat{\mathbf{V}}_{zs} \in \mathbb{C}^{M_x \times L}$  is the estimated signal subspaces for the z-axis subarray, whereas  $\hat{\mathbf{\Gamma}}_{zs} \in \mathbb{C}^{L \times L}$  is the diagonal matrix containing the eigenvalues  $\gamma_1, \gamma_2, \cdots, \gamma_L$  corresponding to the signal subspaces. As the signal power is the same for the subarrays in both axes, we develop a minimization problem to determine the azimuth angles in a sequential manner where  $\gamma_1 > \gamma_2 > \cdots > \gamma_L$ .

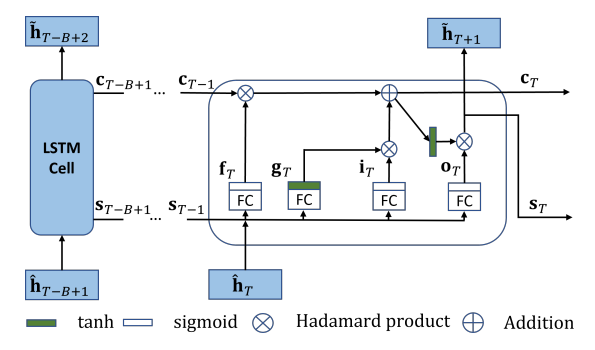


**Fig. 3**: LSTM structure for  $h_{T+1}$  estimation.

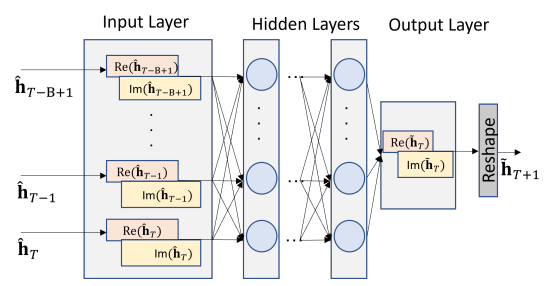


**Fig. 4**: MLP structure for  $h_{T+1}$  channel estimation.

The azimuth angles are then estimated from the following optimization problem:

$$\hat{\boldsymbol{\phi}} = \arg\min_{\varphi_l \in [-\frac{\pi}{2}, \frac{\pi}{2}]} \| (\hat{\mathbf{R}}_{x_{\text{RIS}}} - \sigma_n^2 \mathbf{I}_{W_x}) - \mathbf{A}_x (\hat{\boldsymbol{\phi}}, \hat{\boldsymbol{\theta}}) \hat{\mathbf{R}}_s \mathbf{A}_x (\hat{\boldsymbol{\phi}}, \hat{\boldsymbol{\theta}})^{\text{H}} \|,$$

$$\tag{10}$$

where  $\mathbf{A}_x(\hat{\phi},\hat{\theta}) = [\mathbf{a}_x(\hat{\varphi}_1,\hat{\vartheta}_1),\cdots,\mathbf{a}_x(\hat{\varphi}_L,\hat{\vartheta}_L)] \in \mathbb{C}^{M_x \times L}$ . Finally, the uplink channel gain  $\beta_l$  of each path can also be separately estimated [14]. As a result, for the T-th time frame (n=1), the user-RIS multipath channel  $\mathbf{h}_T$  is reconstructed according to (4).

#### 3.2. RIS-assited User-RIS Channel Prediction

This section presents a deep machine learning-based algorithm for predicting channel  $\mathbf{h}_{T+1}$  exploiting an LSTM network. To handle long-term dependencies, the LSTM network is enhanced by the addition of memory cells and multiplicative gates that regulate the flow of information, as illustrated in Fig. 3.

At each time step, the memory cell generates the output based on the input, which is the estimated channel and the hidden state feedback from the previous time step. Unrolling the network through time, as shown in Fig. 3, the memory cell generates two internal states at time step T: the short-term state  $\mathbf{s}_T$  and the long-term state  $\mathbf{c}_T$ . Traversing the cell from left to right,  $\mathbf{c}_{T-1}$  discards some old memories at the forget gate, integrates new memories selected by the input gate, and then transmits it as the long-term state  $\mathbf{c}_T$  for the next time step T+1.

The current input vector  $\hat{\mathbf{h}}_T$  and the previous short-term memory  $\mathbf{s}_{T-1}$  are input to four different fully connected (FC) layers to produce the activation vectors of gates [15]:

$$\mathbf{f}_T = \sigma_q(\mathbf{W}_f \hat{\mathbf{h}}_T + \mathbf{U}_f \mathbf{s}_{T-1} + \mathbf{b}_f), \tag{11}$$

$$\mathbf{i}_T = \sigma_q(\mathbf{W}_i \hat{\mathbf{h}}_T + \mathbf{U}_i \mathbf{s}_{T-1} + \mathbf{b}_i), \tag{12}$$

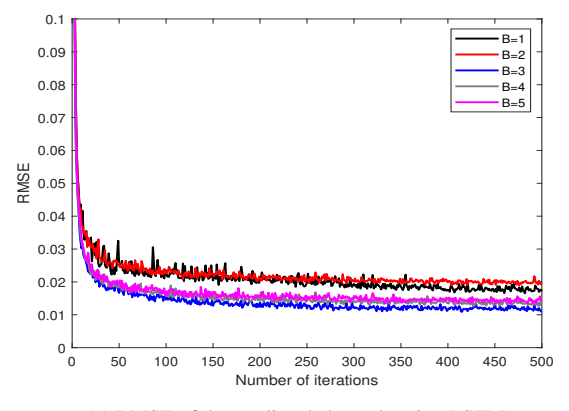
$$\mathbf{o}_T = \sigma_g(\mathbf{W}_o \hat{\mathbf{h}}_T + \mathbf{U}_o \mathbf{s}_{T-1} + \mathbf{b}_o), \tag{13}$$

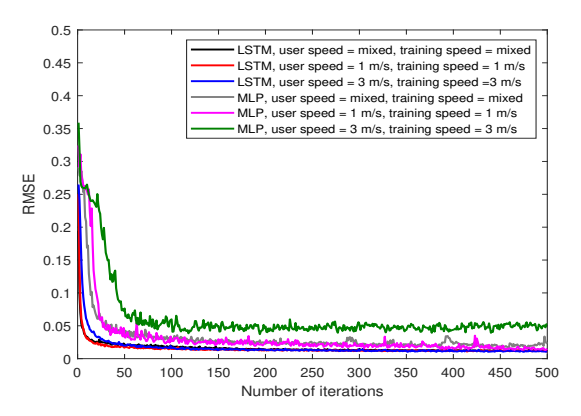
where subscripts f, i, and o correspond to the forget, input, and output gates, respectively,  $\mathbf{W}$  and  $\mathbf{U}$  with appropriate subscripts represent the weight matrices for the FC layers respectively corresponding to the current input vector  $\hat{\mathbf{h}}_T$  and the previous short-term state  $\mathbf{s}_T$ , whereas  $\mathbf{b}$  with appropriate subscripts stands for the bias vector.  $\sigma_g$  denotes the sigmoid activation function.

We can fine-tune these gates in accordance with the rate of channel variations, and this adaptability empowers the LSTM network with robustness compared to memoryless networks like MLPs. By discarding some old memories and incorporating new ones, the previous long-term memory  $\mathbf{c}_{T-1}$  of the LSTM network is updated as

$$\mathbf{c}_T = \mathbf{f}_T \otimes \mathbf{c}_{T-1} + \mathbf{i}_{T-1} \otimes \sigma_h(\mathbf{W}_g \hat{\mathbf{h}}_T + \mathbf{U}_g \mathbf{s}_{T-1} + \mathbf{b}_g), \quad (14)$$

where  $\sigma_h$  denotes the hyperbolic tangent function. Next, the long-term state  $\mathbf{c}_T$  is passed through the hyperbolic tangent function and





(a) RMSE of the predicted channels using LSTM

(b) RMSE of the predicted channels using LSTM and MLP

Fig. 5: Simulated RMSE performance of the predicted channels.

is then filtered by the output gate to produce the short-term state and the output.

The MLP-network depicted in Fig. 4 is used for comparison as an example of memoryless machine learning prediction models [23]. To prepare the dataset for network training, we concatenate consecutive channels as  $\mathbf{v} = [\mathbf{h}_{T-B+1}^{\mathrm{T}}, \cdots, \mathbf{h}_{T}^{\mathrm{T}}]^{\mathrm{T}}$ . Denoting  $\mathbf{W}_k$ ,  $\mathbf{b}_k$ , and  $\sigma_k$  as the weights, biases, and activation function of the kth network for  $k = 1, 2, \cdots K$ , the predicted output is obtained as:

$$\tilde{\mathbf{h}}_{T+1} = \sigma_k(\mathbf{W}_k \sigma_{k-1}(\cdots, \sigma_1(\mathbf{W}_1 \mathbf{v} + \mathbf{b}_1) \cdots) + \mathbf{b}_K). \quad (15)$$

During the training phase, the inputs to both LSTM and MLP networks are the channel vectors  $\hat{\mathbf{h}}_{T-B+1}, \hat{\mathbf{h}}_{T-B+2}, \cdots, \hat{\mathbf{h}}_{T}$ , which are estimated using the method described in Section 3.1, and the output is the reference channel vector  $\mathbf{h}_{T+1}$  at the (T+1)-th time slot. Each hidden layer of the MLP consists of 2BM nodes, and the output layer is designed to have a dimension of 2M, corresponding to the real and imaginary parts of the channel vector,  $\text{Re}(\mathbf{h}_{T+1})$  and  $\text{Im}(\mathbf{h}_{T+1})$ , at the (T+1)-th time slot.

# 4. SIMULATION RESULTS

The RIS consists of a total number of 529 elements, with 11 of them being active elements. Each of the two linear subarrays in the L-shaped configuration includes 6 sensors. Active elements are positioned along the x- and z-axes at  $\mathbb{X} = \mathbb{Z} = \{0, 3, 7, 12, 20, 22\}\lambda/2$ . The non-negative lags for the subarrays are given by  $\mathbb{D}_{\text{self}}^X = \mathbb{D}_{\text{self}}^Z = \{0, 2, 3, 4, 5, 7, 8, 9, 10, 12, 13, 15, 17, 19, 20, 22\}\lambda/2$ .

With the BS at the origin of the Cartesian coordinates, the RIS is positioned at (30 m, 4 m, 10 m) while the user's initial location is (30 m, 34 m, 1.5 m). The carrier frequency is  $f_c=28\,\mathrm{GHz}$ . L=2 paths are considered between the RIS and the mobile user, and the path loss exponents attributed to the two paths are respectively set as 2.2 and 2.1. The generation of training and testing datasets is carried out based on the user's walking speed, and two scenarios are considered: one at a speed of 1 m/s and the other at 3 m/s. Each time frame spans  $T_n=140$  ms, with a sensing time of 40 ms and data transmission lasting 100 ms. A total of  $\dot{T}=1,000$  samples are employed, and the channel noise power remains fixed at  $\sigma_n^2=-80\,\mathrm{dBm}$ . The evaluation of channel prediction performance is accomplished using the root-mean-square error (RMSE) of the estimated channel states, defined as

$$RMSE = \sqrt{\frac{1}{Q} \sum_{q=1}^{Q} \left\| \hat{\mathbf{h}}_{q,n} - \mathbf{h}_{q,n} \right\|^2}, \tag{16}$$

where Q is the number of independent trials.

To predict the channel,  $N_{\rm train} = 11^3$  training data sets are generated that reflect different user-RIS channels associated with the user's speed, and the ADAM training algorithm is used with a batch size of 32. The transmit power of the mobile user pilot signal used for CSI estimation is 25 dBm.

In Fig. 5a, the RMSE is plotted against the number of iterations for predicted channels using the LSTM for different orders (B) of input channels while the network is trained and tested for a user speed of 1 m/s. As the number of iterations increases, the RMSE of the predicted channels decreases. The figure confirms the number of required input channels to predict an optimum output. It is observed that the predicted channel may not be optimal when the input order is short (B=1 and B=2). Additionally, when the channel order is higher than 3, the network performance slightly degrades due to data overfitting, rendering B=3 the optimum choice for this LSTM network.

The LSTM and MLP networks are trained using different user speeds, i.e., 1 m/s, 3 m/s, and their mixture. Fig. 5b shows the RMSE performance of the test datasets for both the LSTM and MLP networks. The curves labelled "user speed = mixed" correspond to a scenario where the 1 m/s and 3 m/s datasets are combined during training, while during testing, the network randomly selects 20% data from the total dataset based on independent trials for validation purposes. The LSTM network consistently outperforms the MLP counterpart as the output converges with a faster rate and lower steady-state errors. Additionally, while both networks achieve better performance when the same speed data is used for training, training the networks using mixed user speeds provides robust performance for users moving at an unknown and possibly time-varying speed.

## 5. CONCLUSION

The paper proposed a novel approach to enhance the quality of service by utilizing estimated and predicted channel states in an RIS-assisted network. The LSTM network is trained using the CSI from preceding time frames to predict channel conditions, thereby reducing the pilot overhead required for channel estimation. Structured matrix completion and pair-matching methods are employed to enhance the identification of multipath channels using semi-passive RIS. This configuration results in an expanded array aperture and decreased computational load. The simulation results demonstrate the superiority of the proposed approach over other machine learning algorithms in terms of effectiveness and performance.

#### 6. REFERENCES

- [1] L. Wei, C. Huang, G. C. Alexandropoulos, C. Yuen, Z. Zhang, and M. Debbah, "Channel estimation for RIS-empowered multi-user MISO wireless communications," *IEEE Trans. Commun.*, vol. 69, no. 6, pp. 4144–4157, 2021.
- [2] X. Pei, H. Yin, L. Tan, L. Cao, Z. Li, K. Wang, K. Zhang, and E. Björnson, "RIS-aided wireless communications: Prototyping, adaptive beamforming, and indoor/outdoor field trials," *IEEE Trans. Commun.*, vol. 69, no. 12, pp. 8627–8640, 2021.
- [3] M. A. Haider and Y. D. Zhang, "RIS-aided integrated sensing and communication: A mini-review," *Frontiers Sig. Process.*, vol. 3, no. 1197240, pp. 1–8, 2023.
- [4] E. Björnson, Ö. Özdogan, and E. G. Larsson, "Intelligent reflecting surface versus decode-and-forward: How large surfaces are needed to beat relaying?" *IEEE Wireless Commun. Lett.*, vol. 9, no. 2, pp. 244–248, 2019.
- [5] Q. Wu, S. Zhang, B. Zheng, C. You, and R. Zhang, "Intelligent reflecting surface-aided wireless communications: A tutorial," *IEEE Trans. Commun.*, vol. 69, no. 5, pp. 3313–3351, 2021.
- [6] Q. Wu and R. Zhang, "Intelligent reflecting surface enhanced wireless network via joint active and passive beamforming," *IEEE Trans. Wireless Commun.*, vol. 18, no. 11, pp. 5394– 5409, 2019.
- [7] A. Taha, M. Alrabeiah, and A. Alkhateeb, "Enabling large intelligent surfaces with compressive sensing and deep learning," *IEEE Access*, vol. 9, pp. 44 304–44 321, 2021.
- [8] M. Jian and Y. Zhao, "A modified off-grid SBL channel estimation and transmission strategy for RIS-assisted wireless communication systems," in *Proc. Int. Wireless Commun. and Mobile Computing (IWCMC)*, Limassol, Cyprus, June 2020, pp. 1848–1853.
- [9] M. A. Haider, M. W. T. Chowdhury, and Y. D. Zhang, "Sparse channel estimation for IRS-aided systems exploiting 2-D sparse arrays," in *Proc. IEEE Sensor Array and Multich. Sig. Process. Workshop (SAM)*, Trondheim, Norway, June 2022, pp. 31–35.
- [10] X. Hu, R. Zhang, and C. Zhong, "Semi-passive elements assisted channel estimation for intelligent reflecting surface-aided communications," *IEEE Trans. Wireless Commun.*, vol. 21, no. 2, pp. 1132–1142, 2021.
- [11] M. Cui, G. Zhang, and R. Zhang, "Secure wireless communication via intelligent reflecting surface," *IEEE Wireless Commun. Lett.*, vol. 8, no. 5, pp. 1410–1414, 2019.

- [12] M. Hua, L. Yang, Q. Wu, C. Pan, C. Li, and A. L. Swindle-hurst, "UAV-assisted intelligent reflecting surface symbiotic radio system," *IEEE Trans. Wireless Commun.*, vol. 20, no. 9, pp. 5769–5785, 2021.
- [13] X. Song, D. Zhao, H. Hua, T. X. Han, X. Yang, and J. Xu, "Joint transmit and reflective beamforming for IRS-assisted integrated sensing and communication," in *Proc. IEEE Wireless Commun. Netw. Conf. (WCNC)*, Austin, TX, April 2022, pp. 189–194.
- [14] M. A. Haider, Y. D. Zhang, and E. Aboutanios, "ISAC system assisted by RIS with sparse active elements," *EURASIP J. Adv. Signal Process.*, vol. 2023, no. 20, pp. 1–22, 2023.
- [15] W. Jiang and H. D. Schotten, "Recurrent neural networks with long short-term memory for fading channel prediction," in *Proc. IEEE Vehicular Tech. Conf. (VTC2020-Spring)*, Antwerp, Belgium, May 2020, pp. 1–5.
- [16] S. Hochreiter and J. Schmidhuber, "Long short-term memory," Neural computation, vol. 9, no. 8, pp. 1735–1780, 1997.
- [17] H. Kim, Y. Byun, and B. Shim, "LSTM-based RIS phase shift control for V2X communication systems," in *Proc. IEEE Vehicular Tech. Conf. (VTC2022-Fall)*, London, UK/Beijing, China, Sept. 2022, pp. 1–5.
- [18] F. Wu, F. Cao, X. Ni, C. Chen, Y. Zhang, and J. Xu, "L-shaped sparse array structure for 2-D DOA estimation," *IEEE Access*, vol. 8, pp. 140 030–140 037, 2020.
- [19] A. Ahmed and Y. D. Zhang, "Generalized non-redundant sparse array designs," *IEEE Trans. Signal Process.*, vol. 69, pp. 4580–4594, 2021.
- [20] C. Zhou, Y. Gu, X. Fan, Z. Shi, G. Mao, and Y. D. Zhang, "Direction-of-arrival estimation for coprime array via virtual array interpolation," *IEEE Trans. Signal Process.*, vol. 66, no. 22, pp. 5956–5971, Nov. 2018.
- [21] C. Zhou, Y. Gu, Z. Shi, and Y. D. Zhang, "Off-grid direction-of-arrival estimation using coprime array interpolation," *IEEE Signal Process. Lett.*, vol. 25, no. 11, pp. 1710–1714, Nov. 2018
- [22] S. Liu, Z. Mao, Y. D. Zhang, and Y. Huang, "Rank minimization-based toeplitz reconstruction for DoA estimation using coprime array," *IEEE Commun. Lett.*, vol. 25, no. 7, pp. 2265–2269, July 2021.
- [23] M. A. Haider, S. R. Pavel, Y. D. Zhang, and E. Aboutanios, "Active IRS-assisted MIMO channel estimation and prediction," in *Proc. IEEE Int. Conf. Acoust., Speech Signal Process.* (ICASSP), Rhodes Island, Greece, June 2023, pp. 1–5.